Profiles of Low-level Stratus Cloud Microphysics Deduced from Ground-based Measurements

Xiquan Dong and Gerald G. Mace
Meteorology Department, University of Utah

Corresponding author address: Dr. Xiquan Dong, Meteorology Department, University of Utah, 135 S 1460 E Rm 819, Salt Lake City, UT 84112. Email: xdong@met.utah.edu

Abstract. Two methods are developed for inferring the vertical profiles of cloud microphysics in liquid phase or liquid dominant mixed phase stratocumulus clouds. The first method uses cloud liquid water path derived from microwave radiometer observations and a profile of radar reflectivity together with a previously derived layer-mean cloud-droplet effective radius to infer the vertical profiles of cloud liquid water content and effective radius. This algorithm is applicable to overcast low-level stratus clouds that occur during the day. In order to extend the retrieval algorithm to a wider range of conditions, we describe a second method that uses an empirical relationship between effective radius and radar reflectivity based on theory and the results of method 1. During the March 2000 cloud IOP at the ARM SGP site, four low-level stratus cases were intensively observed by the ground-based remote sensors and aircraft in situ instruments resulting in a total of 10 hours of simultaneous data from the two platforms. In spite of the large differences in temporal and spatial resolution between surface and aircraft, the derived cloud properties (method 1) are in excellent agreement with the aircraft data overall for the entire 10-hour period and have similar trends and magnitudes for individual case. On average, the surface-retrieved effective radii from method 1 differed from the corresponding aircraft data by 4% during the 10-hour period. Three additional cases were analyzed for time periods when the aircraft was unavailable. When these additional results are combined with the retrievals from the four in situ cases, a total of 36 hours of surface data are used to derive the empirical relationship required for method 2. The 36-hour surface-derived empirical coefficient is, in general, 11% higher than the 10-hour aircraft-derived coefficient, and the difference for individual cases may be smaller or larger than 11%. Sensitivity studies show that the retrieved cloud-droplet effective radius from method 2 is more sensitive to the variation of radar reflectivity when the radar reflectivity is large, but not strongly dependent on the assumptions made concerning the cloud-droplet number concentration profile and shape of the size distribution.

1. Introduction

Knowledge of the vertical structure of a cloud's microphysical characteristics is important for a variety of reasons. The vertical profiles of cloud-droplet effective radius (r_e) and liquid water content (*lwc*) affect the cloud's interaction with solar and infrared radiation that ultimately contribute to the energy budget at the surface and top of atmosphere (TOA). Knowledge of the microphysical structure also increases our understanding of the process acting to form and maintain these cloud systems. This understanding may lead to improved numerical models and parameterizations of clouds. With the availability of cloud radar and other ground-based measurements from the Department of Energy Atmospheric Radiation Measurement (ARM) program (Stokes and Schwartz 1994), it is now possible to continuously monitor the vertical structure of clouds that occur over these sites and evaluate cloud properties in a statistical sense.

Several algorithms have been developed in recent years that combine millimeter wavelength radar observations with other data sources to derive the microphysical properties of low-level stratus clouds. The multi-parameter algorithms developed for low-level liquid-phase stratus clouds use radar reflectivity observations and microwave radiometer-derived cloud liquid water path (*lwp*) combined with various assumptions to retrieve the microphysical properties of the cloud layer. Since these techniques tend to assume a functional form (lognormal or gamma) for the particle size distribution, three independent parameters are generally needed to estimate the characteristics of the particle size distribution. These algorithms can be classified into those that use the solar transmission as additional independent information, such as Dong et al. (1997, 1998, hereafter D97, D98) and Mace and Sassen (2000), and those that do not use the solar transmission but apply additional assumptions, such as Frisch et al. (1995, 1998, hereafter F95, F98). The solar transmission-based algorithms, because they use additional information, can be shown to be more accurate (Mace and Sassen 2000) but these algorithms can only be applied in a narrow range of conditions (daytime). Those algorithms that do not use solar transmission but use additional assumptions can be implemented more generally but tend to demonstrate larger error. Our goal in this study is to exploit the strengths of the two basic methodologies and develop a single framework that can be applied to continuous data without regard to the time of day or the existence of higher cloud layers.

2. Data

During March 2000, the ARM program conducted an Intensive Observational Period (IOP) at the ARM Southern Great Plains (SGP, lat=36.61^{o}N, long=97.5^{o}W) site to obtain comprehensive ground-based measurements of clouds in conjunction with flights of the University of North Dakota Citation research aircraft. One of the goals of this IOP was to validate ground-based retrievals of cloud microphysics using aircraft in situ measurements. The March 2000 cloud IOP was a very successful field experiment with a wide variety of cloud types observed during the four-week period. During the IOP, four low-level stratus cases (March 3, 17, 19, and 21) were intensively observed by the ground-based remote sensors and aircraft instruments resulting in a total of 10 hours of simultaneous data from the two platforms. Three additional cases during the IOP (March 14, 15, and 29) were analyzed for time periods when the aircraft was unavailable. When these additional results are combined with the retrievals from the four in situ cases, a total of 36 hours of surface data are used to derive the empirical relationship between cloud-droplet effective radius and radar reflectivity from a statistical point of view.

Among the ground-based instrument suite, the millimeter-wave cloud radar [MMCR] is the centerpiece. The MMCR operates at a wavelength of 8 mm (35 GHz) in a vertically pointing mode, and provides continuous profiles of radar reflectivity of hydrometeors advecting through the radar field of view (Moran et al. 1998). The cloud top height (Z_t) is derived from cloud radar reflectivity profile, while the cloud base height (Z_b) is derived from a laser ceilometer. Because the radar is quite sensitive at these short ranges (~-55 *dBZ* at 1 km), a few larger precipitation sized droplets that are insignificant to the overall water content and optical path can mask the actual cloud base. Since the laser ceilometer is sensitive to the 2nd moment of the particle distribution instead of the 6th like the MMCR, the ceilometer provides a more faithful estimate of cloud base. The vertical resolutions of radar-derived cloud top height and ceilometer-derived cloud base height are 45 m and 8 m, respectively. The cloud *lwp* is retrieved from the microwave radiometer brightness temperatures measured at 23.8 and 31.4 GHz using a statistical retrieval method (Liljegren et al. 2001). The root-mean-square (RMS) accuracies of the retrievals are about 20 g m^{-2} and 10% for cloud LWP below and above 200 g m^{-2}, respectively (Dong et al. 2000; Liljegren et al. 2001).

The University of North Dakota Citation research aircraft carried a number of Particle Measuring Systems (PMS) probes to provide in situ measurements of the cloud microphysical properties at a 4 Hz sampling rate. Cloud droplet spectra were measured with a PMS Forward Scattering Spectrometer Probe (FSSP-100) and were averaged to 1 Hz for this study. The FSSP probe sized and counted individual particles in 15 diameter bins, with bin centers from 4.4 to 52.3 μm. Corrections to particle concentrations have been applied to account for probe activity and coincidence (electronic dead time) (Baumgardner et al. 1985) and for variations in the effective beam diameter (Dye and Baumgardner 1984). Corrections to particle sizes to account for electronic response time and beam inhomogeneity follow Baumgardner and Spowart (1990). The sizing correction scheme redistributes (re-bins) the counts, and the bin widths have been adjusted to account for ambiguities in the Mie scattering curve. Cloud liquid water content (*lwc*) was calculated from each FSSP spectrum, and effective radius (r_e) was computed as the ratio of the third to the second moment of the cloud particle size spectrum.

Based on the previous studies (e.g. Baumgardner 1983; Dye and Baumgardner 1984; Baumgardner et al. 1985), Miles et al. (2000) summarized all possible errors for FSSP measurements. They are: 1) inhomogeneity across the length and width of the laser beam, which introduces sizing errors; 2) a limited response time in the detector electronic, which can lead to considerable underestimates of cloud-droplet number concentration (*N*); 3) coincident counts, which may underestimate *N* and overestimate r_e, 4) the propagation of error from particle concentrations and size to volume estimates, which can lead to large error to *lwc*, and 5) uncertainties associated with the calibration technique. The overall uncertainties in r_e, *N*, and *lwc* are 14%, 25%, and 30%, respectively when all possible corrections are made to the measurements.

3. Methods

a. Reliance on solar transmission (M1)

D97 used a δ2-stream radiative transfer model in conjunction with ground-based measurements of the cloud boundaries and retrieved *lwp* to retrieve the layer-mean cloud-droplet effective radius ($\overline{r_e}$). The D97 scheme is based on an iterative approach that varies $\overline{r_e}$ in the radiative transfer

calculation until the modeled solar transmission matches the measured value. D98 parameterized the retrieval process using the *lwp*, solar transmission, and cosine of solar zenith angle as

$$\overline{r_e} = -2.07 + 2.49lwp + 10.25\gamma - 0.25\mu_0 + 20.28lwp\gamma - 3.14lwp\mu_{0,} \quad (1)$$

where the units of $\overline{r_e}$ and *lwp* are μm and 100 g m^{-2}, respectively. Error analysis using aircraft data showed the retrieved (D97) and parameterized (D98) values of $\overline{r_e}$ to have uncertainties of 7% and 15% respectively.

Following the development of F95, the radar reflectivity *Z(h)* can be expressed as

$$Z(h) = 2^6 N < r^6(h) >= 2^6 N r_m^6(h)\exp(18\sigma_X^2), \quad (2a)$$

where r_m is the median radius and σ_X is the logarithmic width of the size distribution. Using the fundamental expression for effective radius $r_e(h)$

$$r_e(h) = \frac{< r^3(h) >}{< r^2(h) >} = r_m(h)\exp(2.5\sigma_X^2), \quad (2b)$$

(2a) can be written

$$Z(h) = 2^6 10^{-12} N r_e^6(h)\exp(3\sigma_X^3). \quad (2c)$$

The units of $r_e(h)$, *Z(h)*, and *N* are μm, mm^6/m^3, and cm^{-3}, respectively. The cloud liquid water content (*lwc*) at a given height can be expressed as

$$lwc(h) = \frac{4}{3}\pi\rho_w N r_e^3(h)\exp(-3\sigma_X^2), \quad (3a)$$

where ρ_w is the density of liquid water (10^6 g m^{-3}) and the unit of *lwc(h)* is g m^{-3}. Combining (3a) with (2c) by eliminating $r_e(h)$ and collecting constant terms yields

$$lwc(h) = \frac{\pi}{6}\exp(-4.5\sigma_X^2)[NZ(h)]^{1/2}. \tag{3b}$$

The *lwp* equation can be similarly expressed as

$$lwp = \frac{4\pi}{3}\rho_w N\overline{r_e^3}\exp(-3\sigma_X^2)\Delta H, \tag{4a}$$

or integrating (3b) from cloud base to cloud top

$$lwp = \sum_{base}^{top} lwc(h)\Delta h = \frac{\pi}{6}\exp(-4.5\sigma_X^2)N^{1/2}\Delta h\sum_{base}^{top} Z^{1/2}(h), \tag{4b}$$

where Δh is the radar range gate spacing (90 m in this study), ΔH is cloud thickness (m) - the difference between the MMCR-derived cloud top height and the ceilometer-derived cloud base height, and the unit of *lwp* is g m^{-2}. Solving for $N^{1/2}$ from (4b) and substituting into (3b), the *lwc* at a given range gate then becomes

$$lwc(h) = \frac{lwp}{\Delta h}\frac{Z^{1/2}(h)}{\sum_{base}^{top} Z^{1/2}(h)}. \tag{5}$$

Equation 5 is identical to Eq. (9) of F98. The cloud-droplet effective radius at a given range gate can be derived from (3a)

$$r_e(h) = \left[\frac{lwc(h)}{\frac{4\pi}{3}\rho_w N}\right]^{1/3}\exp(\sigma_X^2). \tag{6a}$$

Solving for N from (4a) and substituting N and *lwc(h)* from (5) into (6a), and collecting constant terms, we can write

$$r_e(h) = \overline{r_e}\left[\frac{\Delta H}{\Delta h}\frac{Z^{1/2}(h)}{\sum_{base}^{top} Z^{1/2}(h)}\right]^{1/3}. \tag{6b}$$

As a result of the assumptions of constant N and σ_X with height (see the appendix), we note that both (5) and (6b) are independent of N and σ_X. Our assumption of a single mode lognormal size distribution should be also kept in mind since the retrieval results can be significantly affected by bimodal size distributions, such as when drizzle is present in the cloud layer.

b. Solar transmission independent (M2)

During the night, when optically thick cirrus or mid level clouds exist above low-level stratus clouds, and in broken stratus conditions, it is impossible to use D98 to estimate the layer-mean cloud-droplet effective radius ($\overline{r_e}$) and to use *M1* to estimate the vertical profile of particle size $r_e(h)$. To provide the cloud property estimates for these conditions, an empirical relationship between effective radius $r_e(h)$ and radar reflectivity *dBZ(h)* can be utilized.

To understand the physical meanings between $r_e(h)$ and *dBZ(h)*, we take $10*\log_{10}$ of both sides of (2c) to change *Z(h)* to *dBZ(h)*. We obtain

$$10\log Z(h) = 10\log[2^6 10^{-12} N r_e^6(h)\exp(3\sigma_X^2)], \tag{7a}$$

which can be written

$$dBZ(h) = 10[1.806 - 12 + 0.4343\ln N + 2.606\ln r_e(h) + 1.303\sigma_X^2]. \tag{7b}$$

Solving for $r_e(h)$,

$$r_e(h) = \frac{\exp(3.912 - 0.5\sigma_X^2)}{N^{0.167}} \exp[0.0384 dBZ(h)] = a \exp[0.0384 dBZ(h)]. \qquad (7c)$$

As can be seen in (7c), there is reason to expect a well-defined functional relationship between $r_e(h)$ and $dBZ(h)$ with the shape of the function governed by the exponential term (A. Frisch, personal communication, 2000). We find that the relationship between effective size and radar reflectivity is straightforward within the theoretical framework established above for vertically constant N and σ_X. However, from profile to profile, a is not necessarily constant but depends on the characteristics of the particle size distribution that are driven by such factors as cloud condensation nuclei (CCN) number and activity spectrum, updraft velocities and the water vapor supersaturation. Therefore, it is reasonable to assume that a will show some dependence on meteorological factors and perhaps on factors as diverse as the location of the airmass source region in the sense that it influences the nature of the CCN spectrum.

To further explore the physical meanings of the regression constant a, consider Fig. 1. To produce Fig. 1, (7c) is used to assess the sensitivity of r_e to σ_X with fixed N (=200 cm^{-3}, Fig. 1a), and to N with fixed σ_X (=0.4, Fig. 1b). Figure 1 also includes the FSSP-measured effective radius and FSSP-calculated radar reflectivity to compare with the theoretical calculations from (7c). As Fig. 1b illustrates, the regression constant a does show a large variation from 15 to 24, and most of the FSSP concentration measurements are between 50 and 800 cm^{-3} with fixed σ_X (=0.4). Figure 1 also demonstrates that r_e is more sensitive (in an absolute sense) to the variation of radar reflectivity when the radar reflectivity is large. For example, from –60 to –30 *dBZ*, r_e only increases 4 μm from 2 to 6 μm (~ a factor of 3 increase), while r_e increases 14 μm from 6 to 20 μm (~ a factor of 3 increase too) when the radar reflectivity increases from –30 to 0 *dBZ*. Figure 1 also suggests that the regression constant a and associated r_e are not a strong function of N and σ_X. For example, the regression constant a varies by about 10% when σ_X changed ±0.2 to the fixed σ_X (=0.4) (Fig. 1a), and about 12% when N varied over a factor of 2 centered on 200 cm^{-3} (Fig. 1b).

We consider two possible levels of approximation for applying *M2*. The coefficient a in (7c) can be derived from a large sample of aircraft data or from the results of *M1* applied over many cases. The coefficient a will be denoted $\bar{a}$ in this circumstance. Using $\bar{a}$, *M2* can be expected to capture the

broadest details of the physical processes that relate the characteristics of the size distribution as expressed in (7c). A more exact degree of approximation is only possible for a particular cloud event when a sufficiently large number of profiles are available to compile a representative regression constant *a*. We will subscript *a* with the symbol *i* (a_i) to denote its derivation for a particular event. The calculated effective radius for a particular cloud event using (7c) with a case-dependent value a_i should be somewhat more accurate than using $\bar{a}$ because a_i would be arguably be better able to characterize the local atmospheric conditions for that cloud event. This approach allows us to provide retrievals of cloud microphysical properties under general conditions and with more accuracy (as discussed below) that has not been possible in the past.

In an operational framework it is important to ensure that the assumptions under which these algorithms were derived are reasonable. To provide more accurate $\overline{r_e}$ values from D98 for the solar transmission-based *M1*, only low-level stratus clouds are selected that satisfy the following five criteria. They are 1) μ_0 is larger than 0.2, 2) the range of γ is 0.1 to 0.7, 3) *lwp* is between 20 and 600 g m^{-2}, 4) cloud top height is less than 3 km, and 5) the range of radar reflectivity (*dBZ*) is –60 to 0. Justification for these 4 can be found in Dong et al. (2000). Criterion 5 is based on the radar reflectivity calculated from the aircraft FSSP measurements during the IOP. In an operational framework, we apply *M1* to daytime and overcast stratus events when they satisfy the five criteria listed above, and *M2* to other times.

The radar reflectivity is dominated by heavy drizzle droplets (median radius greater than 60 μm, F95) when the radar reflectivity is more than 0 *dBZ*. F95 and Mace and Sassen (2000) have demonstrated that light drizzle is frequently found when the radar reflectivity factor rises much above –20 *dBZ* with a cumulative probability of ~20% at 0 *dBZ* (Fig. 3 of F95). Between –20 and 0 *dBZ*, there is overlap between large cloud droplets and a precipitation mode composed of light drizzle. The presence of heavy drizzle (*dBZ* >0) in clouds certainly influences the radar reflectivity measurements and the microwave radiometer brightness temperature. The existence of light drizzle also causes some additional bias in our retrievals, but this error is not always significant as proposed by Mace and Sassen (2000) and F95 as shown in Figs. 2-3. The FSSP is designed for measuring cloud droplets with a maximum mean radius of 26 μm (corresponding r_e ~35 μm). We find that volumes with a reflectivity factor near 0 *dBZ* correspond to effective radii of about 20 μm

from both the surface and aircraft data in this study as shown in Fig. 3. Cloud droplets with radii smaller than 20 μm principally grow from water vapor condensation rather than collision coalescence (Duynkerke et al. 1995).

4. Results and Discussion

Four low-level stratus cases (March 3, 17, 19, and 21) were observed by ground-based remote sensors and aircraft instruments during the March 2000 cloud IOP at the ARM SGP site. Three additional stratus cases during the IOP (March 14, 15, and 29) were observed from the ground-based remote sensors only with a total of 36 hours of data. Since the cloud temperatures of the four aircraft-supported cases were near or greater than 0 °C, we assume that no ice was present in the clouds. The surface data have been averaged to 5-min resolution with a total of 10 hours of simultaneous data collected from the airborne and ground-based platforms for the four cases. To compare the aircraft and surface results from a statistical point of view and to derive a representative empirical relationship between r_e and *dBZ*, a total of 10 hours of aircraft data and 36 hours of surface data during the IOP are used and plotted in Figs. 2-3. More detailed comparisons between the surface retrievals and aircraft FSSP data from three cases (March 3, 17, and 21) are discussed in this section.

a. Empirical coefficients between r_e and dBZ from both the aircraft and surface data (M1)

The empirical coefficients between $r_e(h)$ retrieved by the solar transmission-dependent method (*M1*) and *dBZ(h)* (hereafter r_e and *dBZ*) from both the surface and aircraft data for the four aircraft-supported cases during the March 2000 cloud IOP are shown in Fig. 2. The differences in a_i between the surface and aircraft range from 2% to 23% over the four cases. This magnitude of error is about the magnitude expected from the error in assuming constant N and σ_X. Some of the differences may be also due to the differences in temporal and spatial sampling between the aircraft and surface instruments or to a limited sample size. Using a spectrum of data sets that provides a large number of samples, issues related to a limited sample size can be avoided. However, this, of course, masks the case-to-case variability in a_i that may very well be due to real differences in cloud microphysics.

The aircraft and surface derived coefficients ($\bar{a}$) between r_e and *dBZ* through a large number of samples are shown in Fig. 3 and their frequency distributions are shown in Fig. 4. As Figs. 3-4 illustrated, the empirical coefficients derived from both the surface and aircraft FSSP data agree reasonably well during the IOP, and their mean r_e and Root-Mean-Square (RMS) values are nearly identical. The surface-derived coefficient $\bar{a}$ (=22.0) is about 11% higher than that ($\bar{a}$ =19.5) derived from the FSSP data. This discrepancy may partially result from the sampling difference between the aircraft FSSP and surface radar where the FSSP-measured effective radii sampled from ~3-4 μm as discussed in section 2 and shown in Fig. 3, while the surface-retrieved effective radii between 2 and 4 μm contributed about 8% to the mean value during the IOP (Fig. 4). The averaged value of radar reflectivity measured from the ground-based radar during the IOP is about 4 *dBZ* lower than that calculated from the FSSP data (Fig. 4), which may be due to either the sampling difference between two datasets, the radar calibration, or calibration of the FSSP. The big advantage of *M2* is to bypass radar calibration uncertainties, but it is strongly dependent on the microwave radiometer-derived *lwp.* On average, the surface-retrieved cloud-droplet effective radius (*M1*) differed from the corresponding aircraft in situ measurement by 4% during the 10-hour period, while the 36-hour surface-calculated cloud-droplet effective radius (*M2*) differed from the 10-hour aircraft data by 11% during the IOP. Although the difference in $\bar{a}$ between the aircraft and surface data during the IOP is only 11%, the difference in individual case may be larger than 11%.

b. Validation of the M1 and M2 results using the FSSP data on March 3, 17, and 21

On March 3, with a northerly wind of ~15 m s^{-1} in the boundary layer, the aircraft remained within 20 km of the SGP central facility (SCF) flying a triangular pattern over several additional remote sites distributed in a small array northeast and east of the SCF. Early in the flight, the aircraft flew towards the SCF from the northeast, then slowly descended from cloud top to cloud base and quickly climbed back to cloud top in the triangle pattern. At around 18.3 UTC, the aircraft flew northward from the SCF in the middle of cloud and returned to the SCF from the northeast at 18.7 UTC. It then repeated the triangle pattern, used at the beginning of the flight, until 20.0 UTC.

As shown in Fig. 5, the ceilometer-measured cloud base was near 0.5 km, while the radar-derived cloud top height varied from 1 to 1.5 km during the 3-hour period. The radar data were missing from 18.5 to 19.0 UTC. Overall, the surface-retrieved r_e values (5-min resolution) from both *M1*

and *M2* (using the surface-derived regression constant $\bar{a}$ =22 during the IOP) agree very well as shown in Figs. 5b-5c, and they also have good agreement with the aircraft FSSP data (1-min resolution) (Figs. 5d-5e). The FSSP-derived *lwc* and r_e were averaged to 1-min resolution to have the best match with the surface retrievals at each radar range gate. The surface retrievals from *M1* in Figs. 5d-5e were selected when they were at the same altitude as the aircraft in the cloud (±50 m). We note that this may not be a perfect match between the aircraft data and the surface retrievals because the aircraft did not sample directly above the surface site. As demonstrated in Figs. 5d-5e, the surface-retrieved *lwc* and r_e closely follow the trend of FSSP data, and their frequency distributions (Fig. 6) from the available data sets in Figs. 5d-5e also agree very well with the frequency distributions of FSSP data. Overall, the good agreement is encouraging, and suggests that both the FSSP data and the surface retrievals are capable of characterizing nearly the same cloud microphysics as a function of height and time during this cloud event.

To further validate the surface retrievals from both *M1* and *M2*, eight profiles of cloud *lwc* and r_e from the FSSP data collected on March 3 are used. The eight profiles were selected from the 17.5 to 19.6 UTC period when the aircraft descended from cloud top to cloud base and lasted at least 5 min to match the surface 5-min temporal resolution for each profile. As shown in Fig. 7, the surface-retrieved *lwc* profiles have excellent agreement with the aircraft FSSP data in magnitude and shape, even at cloud top where entrainment causes rapid changes to the droplet distribution. The Root-Mean-Square (RMS) difference in *lwc* between the FSSP data and the surface retrievals from the eight profiles is 0.104 g m^{-3} (~40% relative to the 0.253 and 0.266 g m^{-3} of FSSP and surface means). The surface-retrieved r_e values from both *M1* and *M2* also agree well with the FSSP data as shown in Fig. 8. The RMS differences in r_e between the FSSP data and the surface retrievals (*M1* and *M2*) are 0.75 and 0.78 μm (~11% relative to the 6.8 μm of FSSP mean), respectively.

The cloud properties on March 21 are similar to those observed in the March 3 case. The stratus cloud advected northward in a southerly flow at approximately of 10 m s^{-1}. The flight pattern of this case consisted primarily of "S" pattern flown over the SGP central facility and supplemental facilities within 20 km of the SCF. As shown in Fig. 9, there are apparently two quite different cloud layers, with very different cloud microphysics. The cloud base and top heights of the lower

layer are around 0.5 and 1.5 km, respectively, at 17.0 UTC. After 17.5 UTC, the cloud base height increased and cloud top height remained nearly constant. By 19.0 UTC, the lower layer merged with the upper layer. The cloud base and top heights of the upper layer are approximately 1.5 and 3 km, respectively, at 17.0 UTC. This upper layer starts to break up at 17.5 UTC. The base of the upper layer is gradually replaced or merged with the lower layer, while its top part forms a 100-200 m thick layer at 18.5 UTC. This thin upper layer is apparently the one sampled by the aircraft around 19.0 UTC.

The *lwc* and r_e values of the upper layer are relatively uniform but much smaller than those from the lower layer as demonstrated in Fig. 9. The retrieved *lwc* and r_e profiles from the lower layer, which decrease with height, are very different from our conceptual model and should, therefore, challenge the validity of the algorithm. According to the cloud properties from both the surface retrievals and the aircraft FSSP data at the aircraft altitude in the cloud, we divide the 2.5-hour flight time into five periods. The cloud microphysics from both period 1 (before 17.5 UTC) and period 3 (from 18.2 to 18.9 UTC) represent the cloud properties of the lower layer with the large *lwc* and r_e values. The *lwc* and r_e from both period 2 (from 17.5 to 18.2) and period 4 (from 18.9 to 19.4 UTC) are much smaller than in the lower layer, and represent the cloud properties of the upper layer. The cloud properties from the last period (after 19.4 UTC) represent the combination of the lower and upper layers, and the cloud microphysical values are in between those of the lower and upper layers. The similarity in the frequency distributions of FSSP data and surface-derived cloud properties (*M1*), as well as the nearly identical means (Fig. 10), support the above discussion and suggest that the algorithm is able to accurately characterize cloud properties in circumstances that depart somewhat from the assumed well-mixed stratus-topped boundary layer. The totally different cloud microphysics between periods 1&3 and 2&4 captured by both surface remote sensors and aircraft FSSP can support our conclusion.

On March 17, the cloud moved from south to north at approximately of 10 m s^{-1}. Like the March 21 case, the aircraft flew mostly within 20 km of the SGP central facility in an "S" pattern during the 2.5-hour period. The ground-based ceilometer- and radar-derived cloud base and top heights are 0.3 and 1.7 km, respectively, while the aircraft flew at an altitude of approximately 1 km from 18.2 to 20.5 UTC (Fig. 11). Similar to the March 3 case, the surface retrieved *lwc* and r_e (*M1*) values

scatter around the FSSP data, and basically follow the trend of FSSP data as demonstrated in Fig. 11. The frequency distributions of surface retrieved *lwc* and r_e (*M1*) values are similar to the distributions of FSSP data (Fig. 12). Overall, there is reasonable agreement between the surface retrievals (*M1*) and the aircraft FSSP data. However, unlike the March 3 and 21 cases, the r_e values from *M1* are much larger than from *M2*, especially from 17.5 to 19.0 UTC. This feature is related to the small radar reflectivity (~ -33 *dBZ*) and large cloud *lwp* (> 400 g m^{-2}) during this period, and further study is necessary to understand this aspect of the case study.

5. Conclusions

Two methods have been developed for inferring the vertical profiles of cloud microphysics. The first method uses measurements of cloud liquid water path and a profile of radar reflectivity together with a previously derived layer-mean cloud-droplet effective radius to infer the vertical profiles of cloud liquid content and effective radius. This algorithm is applicable to overcast low-level stratus clouds that occur during the day. In order to extend the conditions under which the algorithm can be applied, we describe a second method that uses an empirical relationship between effective radius and radar reflectivity based on theory and the results of method 1. We find reasonable agreement between observed and retrieved cloud liquid water content and effective radius using data collected during the March 2000 cloud IOP at the ARM SGP site. On average, the surface-retrieved effective radii from methods 1 and 2 differed from the corresponding aircraft data by 4% and 11%, respectively. For the more detailed comparisons of three cases, the overall good agreement is encouraging, and suggests that both the FSSP data and the surface retrievals are capable of characterizing nearly the same cloud microphysics as a function of height and time during these cloud events. The totally different cloud microphysics between periods 1&3 and 2&4 in the March 21 case captured by both surface remote sensors and aircraft FSSP can support our conclusion.

These methods, combined with previously developed methods (Dong et al. 1998), have been integrated into a single framework to provide the vertical profiles and layer-mean cloud microphysical properties of low-level stratus clouds; we apply method 1 during daytime and overcast low-level stratus clouds, and method 2 for other cloud conditions such as at night and during multiple layer situations. However, given the sensitivity of the coefficient *a* to the

characteristics of the particle size distribution, the application of method 2 to other time periods and other sites should be done with caution.

Acknowledgments. The surface-based data were obtained from the Atmospheric Radiation Measurement (ARM) Program sponsored by the U.S. Department of Energy (DOE), Office of Energy Research, Office of health and Environmental Research, and Environmental Sciences Division. Special thanks for Ms. S. Benson to process the surface data, Dr. J. Liljegren to reprocess the ground-based microwave radiometer data, and Mr. M. Poellot to provide the aircraft FSSP data. During this study, the authors were supported by the ARM Program under Grant DE-AI02-97ER62341, NASA CERES Program under contract NAG-1-2250, and NASA EOS validation program under contract NAG-5-6458.

Appendix

Constant N and σ_X with height

To retrieve the vertical profiles of cloud microphysical properties, we assume that, 1) the cloud-droplet number concentration (N) is constant with height, 2) the cloud-droplet size distribution can be described with a lognormal function [Eq. (1) in F95], 3) the standard deviation of droplet size distribution is constant with height, and 4) the layer-mean effective radius derived from Eq. (1) is valid. These assumptions have been verified by aircraft data in other studies such as the compilation of Miles et al. (2000), and the case study presented by Sassen et al. (1999) and D98. To further examine the validity of these assumptions, eight profiles of cloud-droplet number concentration (N) and logarithmic width of the distribution (σ_X) from the March 3 aircraft data are presented in Figs. A1-A2. The means and standard deviations of N and σ_X in each profile are calculated in the 90 m interval – the same range gate spacing as the MMCR data we use.

Figure A1 shows that N tends to increase just above cloud base and decreases near cloud top in all profiles. In the center of the cloud, N shows some degree of variability in certain profiles while others remain nearly constant with height. In evaluating this information it is important to note that each vertical profile represents a single ramp from cloud top to cloud base that extends over several horizontal kilometers during which time several cloud cells with updrafts and downdrafts may be sampled. While it is impossible to quantify, some amount of the variability shown in Fig. A1 is due to horizontal structure in the cloud layer. The physical reasons leading to such profiles are related to the fact that the maximum supersaturation is reached within 100 m above cloud base, after which the supersaturation rapidly decreases to a value just above water saturation and few new particles are nucleated. Finally entrainment near cloud top can evaporate most of the small cloud droplets leading to a general decrease in the particle concentration. As Fig. A1 demonstrates, the majority of the 90 m averages vary within about 50% of the calculated layer-mean values in the eight profiles, and significantly, each layer-mean value lies approximately within 1 standard deviation of the average of that vertical interval. This suggests that assuming a constant value of N in the cloud layer is reasonable. The vertical variability of N does lead to error of approximately 10% in our retrieval of particle size.

Figure A2 illustrates that σ_X varies within 1 standard deviation of the average at any given height, and tends to show a different vertical structure to *N*. The decrease of σ_X with height from cloud base can be explained by the traditional theory of condensational growth of droplets in an updraft (Rogers and Yau 1989), whereas the increase near cloud top is mainly due to the entrainment processes (Miles 2000, Mace and Sassen 2000). The assumption of constant σ_X with height results in a 3% retrieval error of particle size.

References

Baumgardner, D., 1983: An analysis and comparison of five water drop measuring instruments. *J. Climate Appl. Meteor.,* **22**, 891-910.

Baumgardner, D., and M. Spowart, 1990: Evaluation of the Forward Scattering Spectrometer Probe. Pat II: Time response and laser inhomogeneity limitations. *J. Atmos. Oceanic Technol.,* **7**, 666-7672.

Baumgardner, D., W. Strapp and J.E. Dye, 1985: Evaluation of the Forward Scattering Spectrometer Probe. Part II: Corrections for coincidence and dead-time losses. *J. Atmos. Oceanic Technol.,* **2**, 626-632.

Dye, J.E., and D. Baumgardner, 1984: Evaluation of the Forward Scattering Spectrometer Probe. Part I: Electronic and optical studies. *J. Atmos. Oceanic Technol.,* **1**, 329-344.

Dong, X., T.P. Ackerman, E.E. Clothiaux, P. Pilewskie, and Y. Han, 1997: Microphysical and radiative properties of boundary layer stratiform clouds deduced from ground-based measurements. *J. Geophs. Res.,* **102**, 23 829-23 843.

Dong, X., T.P. Ackerman, and E.E. Clothiaux, 1998: Parameterizations of microphysical and shortwave radiative properties of boundary layer stratus from ground-based measurements. *J. Geophs. Res.,* **103**, 31 681-31 693.

Dong, X., P. Minnis, T.P. Ackerman, E.E. Clothiaux, G.G. Mace, C.N. Long, and J.C. Liljegren, 2000: A 25-month database of stratus cloud properties generated from ground-based measurements at the ARM SGP site. *J. Geophs. Res.,* **105**, 4529-4537.

Duynkerke, P.G., H. Zhang, and P.J. Jonker, 1995: Microphysical and turbulent structure of nocturnal stratocumulus as observed during ASTEX. *J. Atmos. Sci.,* **52**, 2763-2777.

Frisch, A., C.W. Fairall, and J.B. Snider, 1995: Measurement of Stratus Cloud and Drizzle Parameters in ASTEX with a K-Band Doppler Radar and a Microwave Radiometer. *J. Atmos. Sci.,* **32**, 2788-2799.

Frisch, A., G. Feingold, C.W. Fairall, and T. Uttal, 1998: On cloud radar and microwave radiometer measurements of stratus cloud liquid water profiles. *J. Geophs. Res.,* **103**, 23 195-23 197.

Liljegren, J. C., E.E. Clothiaux, G.G. Mace, S. Kato, and X. Dong, 2001: A new retrieval for cloud liquid water path using a ground-based microwave radiometer and measurements of cloud temperature. *J. Geophys. Res*., **106**, 14 485-14 500.

Mace, G.G., and K. Sassen, 2000: A constrained algorithm for retrieval of stratocumulus cloud properties using solar radiation, microwave radiometer, and millimeter cloud radar data. *J. Geophs. Res.,* **105**, 29 099-29 108.

Miles, N.L., J. Verlinde, and E.E. Clothiaux, 2000: Cloud-Droplet Size Distributions in low-level Stratiform Clouds. *J. Atmos. Sci.,* 57, 295-311.

Moran, K.P., B.E. Martner, M.J. Post, R.A. Kropfli, D.C. Welsh, and K.B. Widener, 1998: An unattended cloud-profiling radar for use in climate research. *Bull. Amer. Meteor. Soc*., **79**, 443-455.

Rogers, R.R., and M.K. Yau, 1989: *A Short Course in Cloud Physics*. 3d ed. Pergamon Press, 293 pp.

Sassen, K., G.G. Mace, Z. Wang, M.R. Poellot, S.M. Sekelskey, and R.E. Mcintosh, 1999: Continental stratus clouds: A case study using coordinated remote sensing and aircraft measurements. *J. Atmos. Sci.,* **56**, 2345-2358.

Stokes, G.M., and S.E. Schwartz, 1994: The Atmospheric Radiation Measurement (ARM) program: Programmatic background and design of the cloud and radiation testbed. *Bull. Amer. Meteor. Soc*., **8**, 1251-1256.

Figure Captions

Fig. 1. Sensitivities of the retrieved r_e to (a) σ_X with fixed N =200 cm^{-3}, and to (b) N with fixed σ_X =0.4. FSSP-measured effective radius vs. FSSP-calculated radar reflectivity during the IOP.

Fig. 2. Empirical coefficients between r_e and *dBZ* from the four aircraft-supported cases during the March 2000 cloud IOP.

Fig. 3. 10 hours of aircraft FSSP data at 1 Hz, and 36 hours of surface data in 5-min resolution during the IOP.

Fig. 4. Frequency distributions of 10 hours of FSSP data and 36 hours of surface data (*M1*) during the IOP.

Fig. 5. Cloud *LWC* (a) and r_e profiles retrieved from *M1* (b) and *M2* (c) (5-min) and aircraft altitude (solid line) in the three upper panels. The 1-min averages of cloud *lwc* (d) and r_e (e) from the aircraft FSSP data (solid line) with corresponded surface retrievals from *M1* (asterisks) at the same altitude in the two lower panels.

Fig. 6. Frequency distributions of FSSP data (solid line) and surface retrievals (dash line) from the available data sets in Figs. 5d-5e.

Fig. 7. Eight *LWC* profiles from the surface (circle) and FSSP data (triangle) were selected during the 17.5-19.6 UTC period on March 3 at the ARM SGP site. Each aircraft profile represented a descending from cloud top to cloud base and lasted at least 5 min to match the surface 5-min temporal resolution and the bars represent the standard deviations of 90-m MMCR vertical resolution.

Fig. 8. Same as Fig. 7 but for r_e profiles from *M1* (circle), *M2* (diamond), and FSSP data (triangle).

Fig. 9. Same as Fig. 5 but on March 21.

Fig. 10. Same as Fig. 6 but on March 21.

Fig. 11. Same as Fig. 5 but on March 17.

Fig. 12. Same as Fig. 6 but on March 17.

Fig. A1. Eight profiles of cloud-droplet number concentration measured by the aircraft were selected during the 17.5-19.6 UTC period on March 3 at the ARM SGP site. Each profile represented a descending from cloud top to cloud base and lasted at least 5 min to match the surface 5-min temporal resolution. The bars represent the standard deviation of 90-m MMCR vertical resolution and dashed lines are the layer means.

Fig. A2. Same as Fig. A1 but for cloud-droplet size distribution (σ_X).

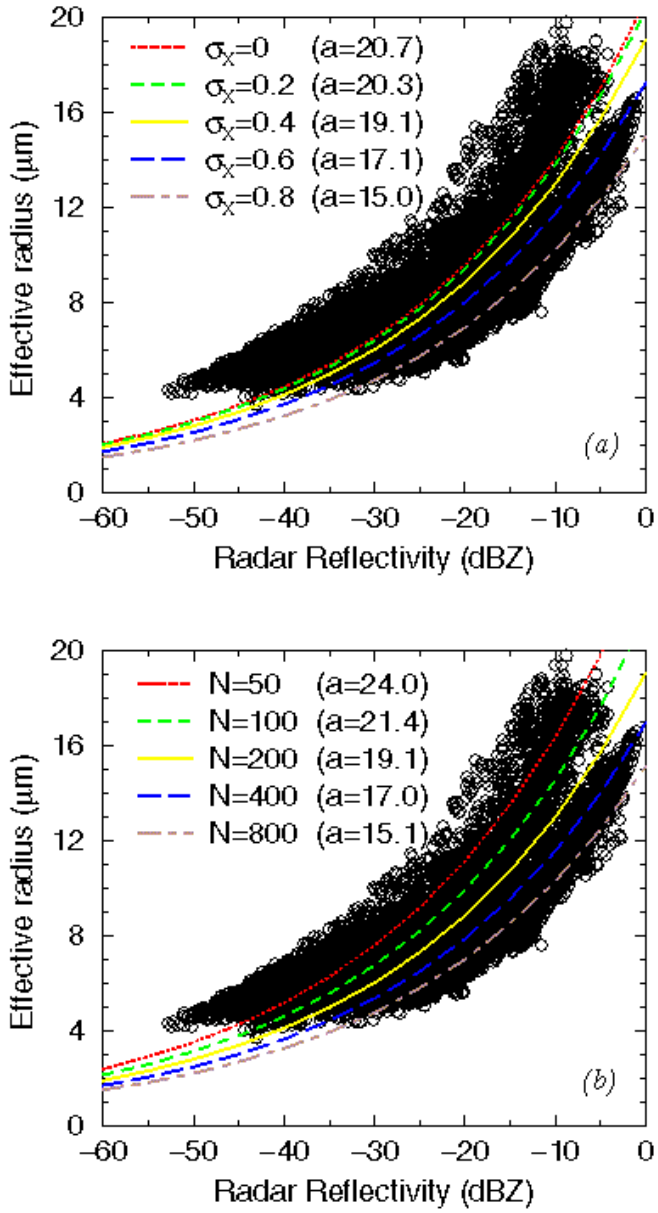
σX=0 (a=20.7)
σX=0.2 (a=20.3)
σX=0.4 (a=19.1)
σX=0.6 (a=17.1)
σX=0.8 (a=15.0)
(a)
Effective radius (μm)
Radar Reflectivity (dBZ)
N=50 (a=24.0)
N=100 (a=21.4)
N=200 (a=19.1)
N=400 (a=17.0)
N=800 (a=15.1)
(b)
Effective radius (μm)
Radar Reflectivity (dBZ)

Figure 1

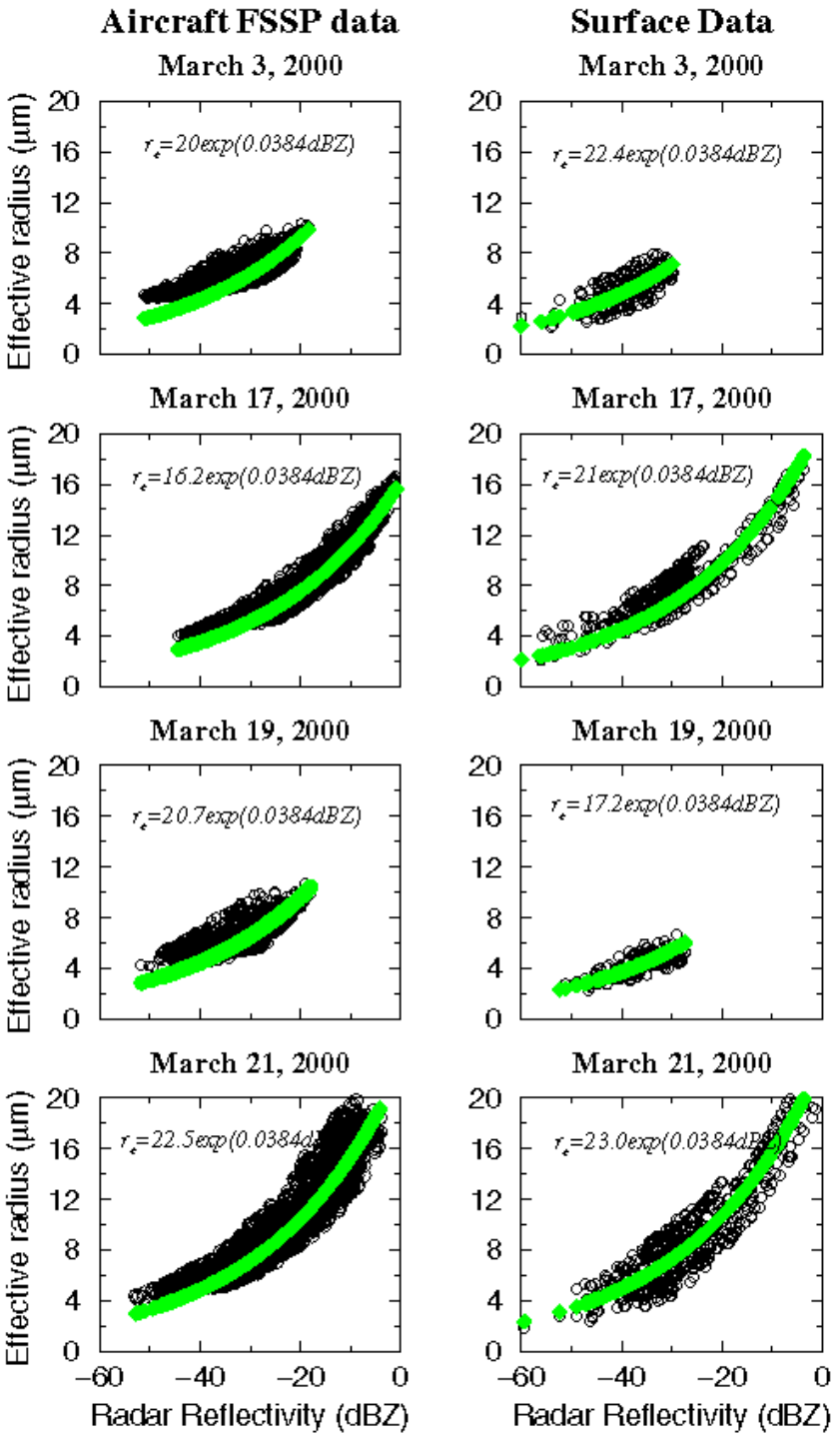
Aircraft FSSP data
Surface Data
March 3, 2000
March 17, 2000
March 19, 2000
March 21, 2000
r_e=20exp(0.0384dBZ)
r_e=22.4exp(0.0384dBZ)
r_e=16.2exp(0.0384dBZ)
r_e=21exp(0.0384dBZ)
r_e=20.7exp(0.0384dBZ)
r_e=17.2exp(0.0384dBZ)
r_e=22.5exp(0.0384d
r_e=23.0exp(0.0384dBZ)
Effective radius (μm)
Radar Reflectivity (dBZ)
0
4
8
12
16
20
−60
−40
−20
0

Figure 2

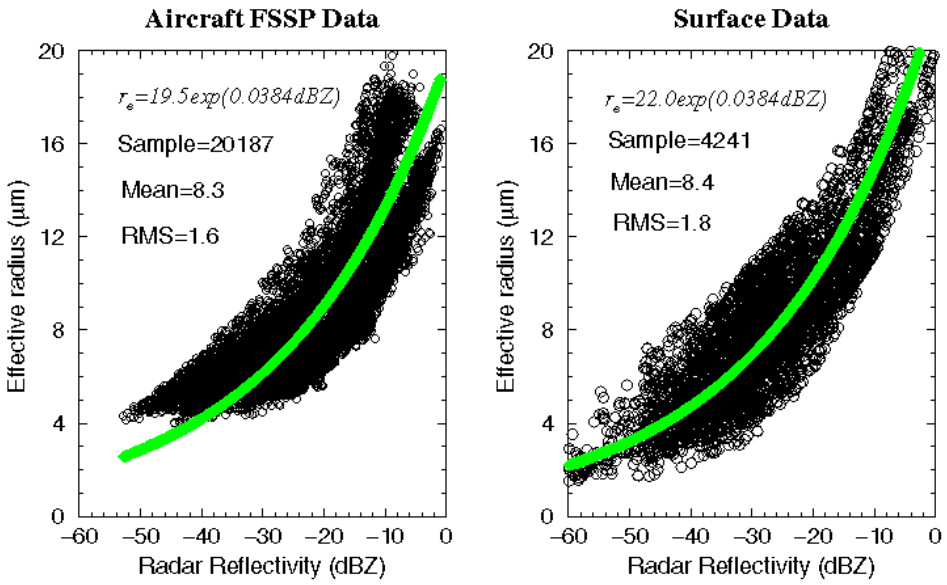
Aircraft FSSP Data
r_e=19.5exp(0.0384dBZ)
Sample=20187
Mean=8.3
RMS=1.6
Effective radius (μm)
Radar Reflectivity (dBZ)
Surface Data
r_e=22.0exp(0.0384dBZ)
Sample=4241
Mean=8.4
RMS=1.8
Effective radius (μm)
Radar Reflectivity (dBZ)

Figure 3

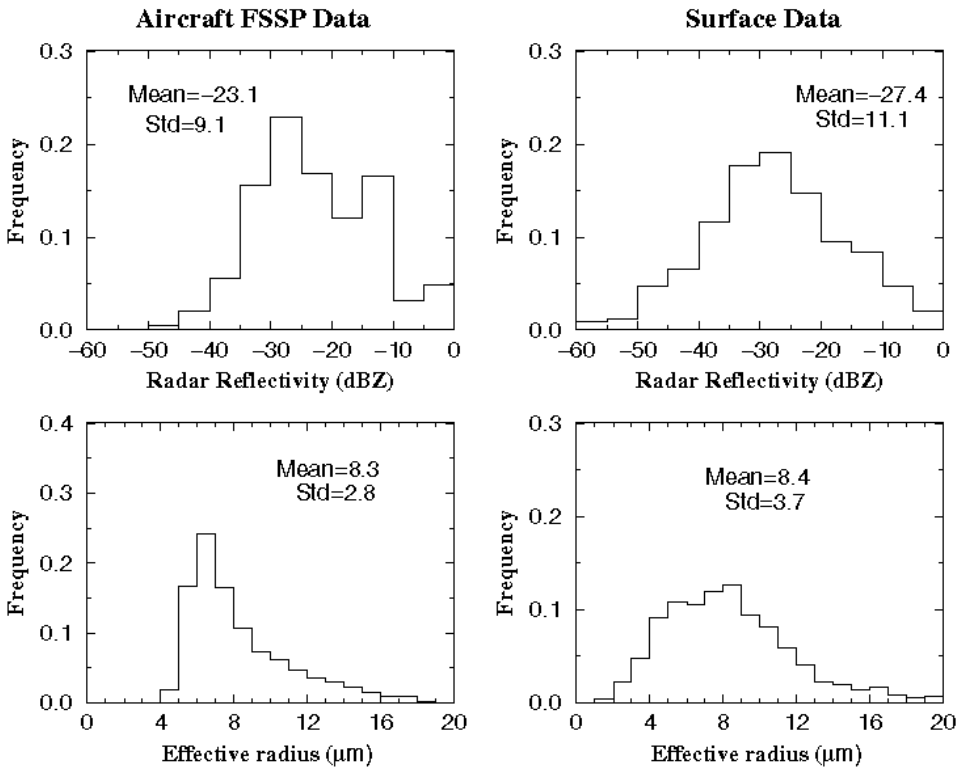
Aircraft FSSP Data
Surface Data
Mean=-23.1
Std=9.1
Mean=-27.4
Std=11.1
Frequency
Radar Reflectivity (dBZ)
Mean=8.3
Std=2.8
Mean=8.4
Std=3.7
Effective radius (μm)

Figure 4

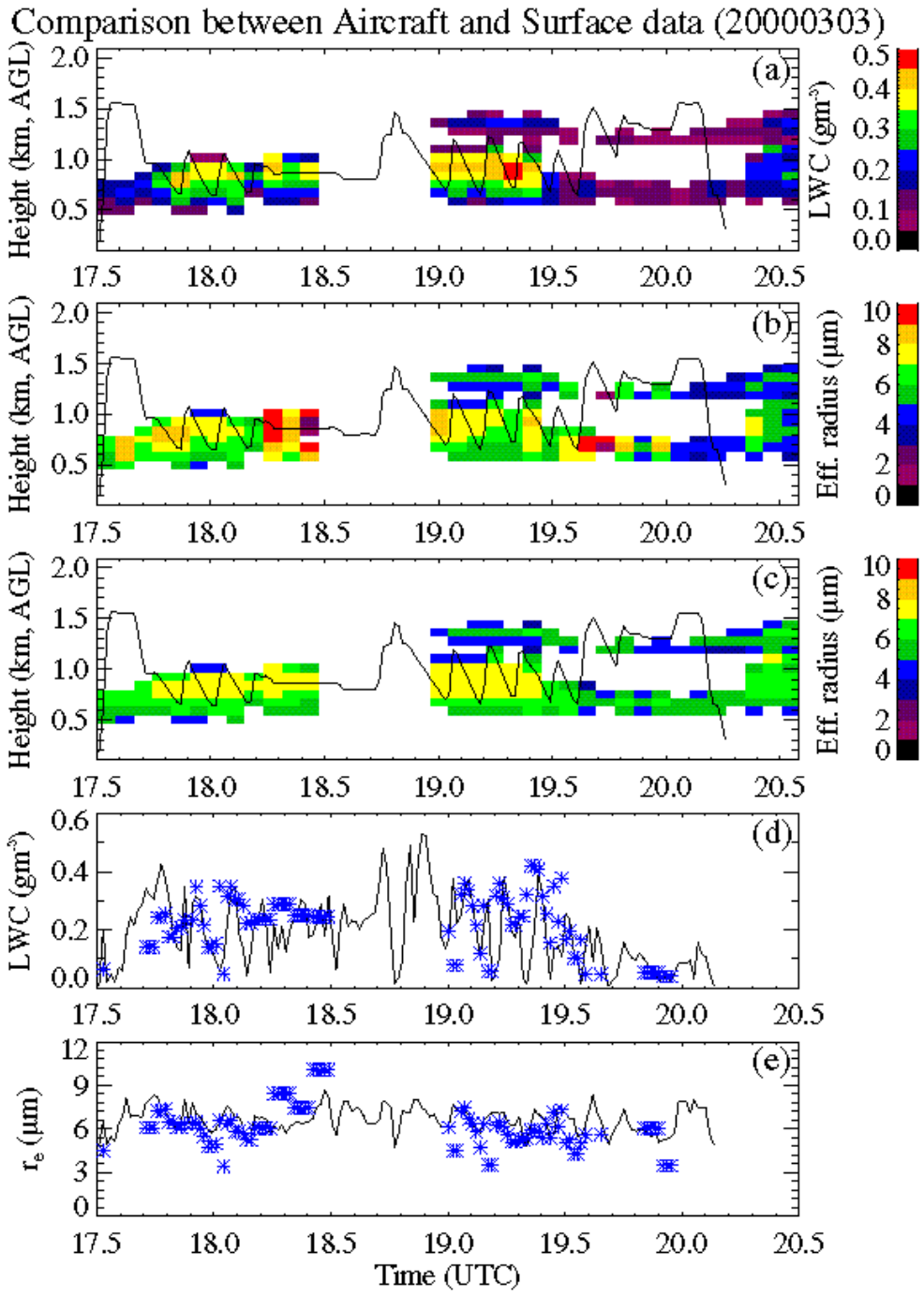
Comparison between Aircraft and Surface data (20000303)
(a)
(b)
(c)
(d)
(e)
Height (km, AGL)
LWC (gm^{-3})
Eff. radius (μm)
r_e (μm)
Time (UTC)
17.5
18.0
18.5
19.0
19.5
20.0
20.5

Figure 5

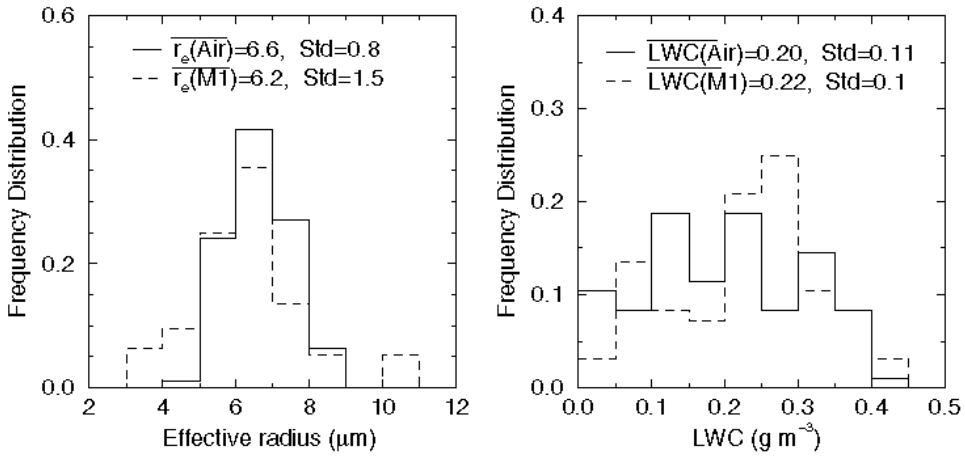
$\overline{r_e}$(Air)=6.6, Std=0.8
$\overline{r_e}$(M1)=6.2, Std=1.5
Frequency Distribution
Effective radius (μm)
$\overline{LWC}$(Air)=0.20, Std=0.11
$\overline{LWC}$(M1)=0.22, Std=0.1
Frequency Distribution
LWC (g m^{-3})

Figure 6

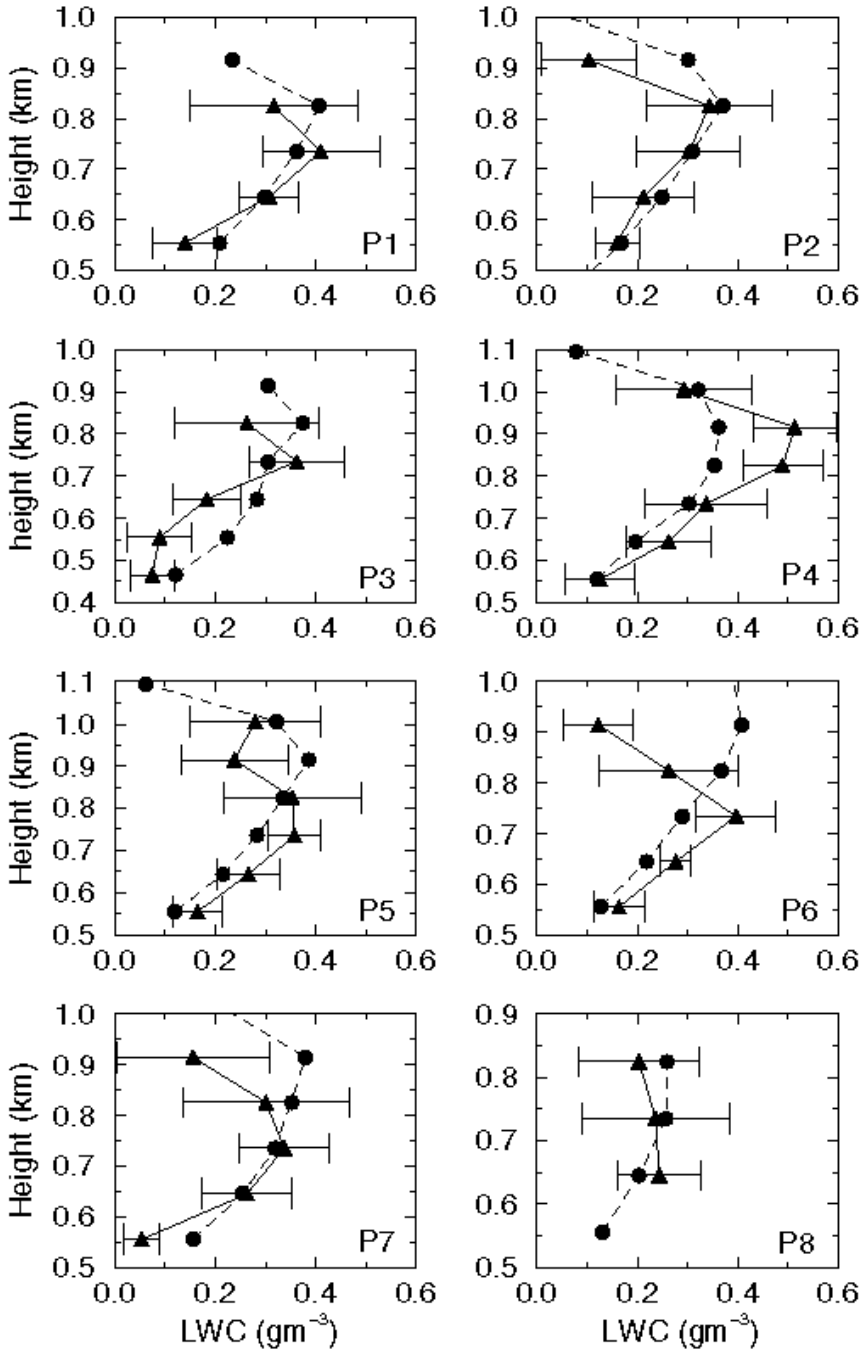

Figure 7

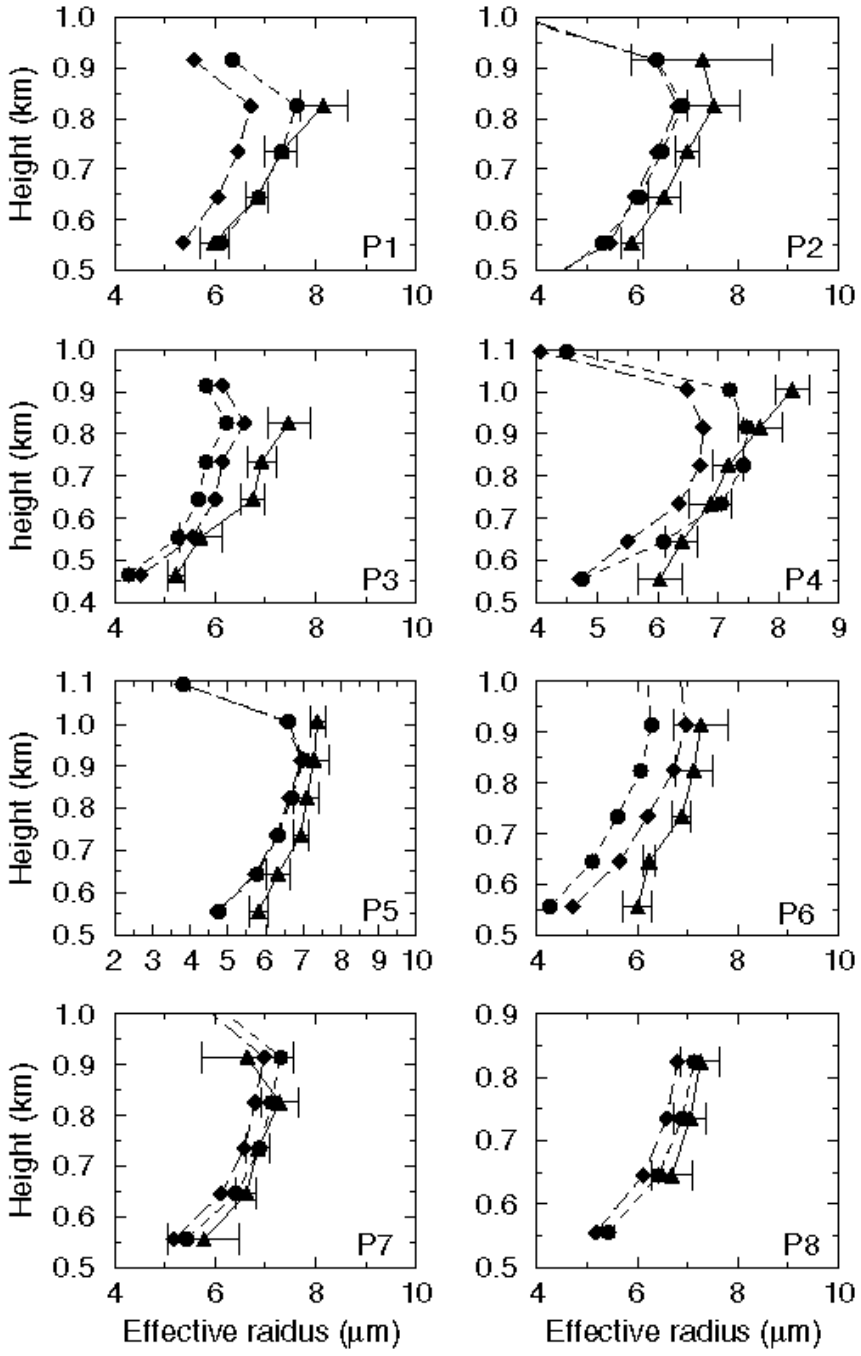
Height (km)
height (km)
P1
P2
P3
P4
P5
P6
P7
P8
Effective raidus (μm)
Effective radius (μm)

Figure 8

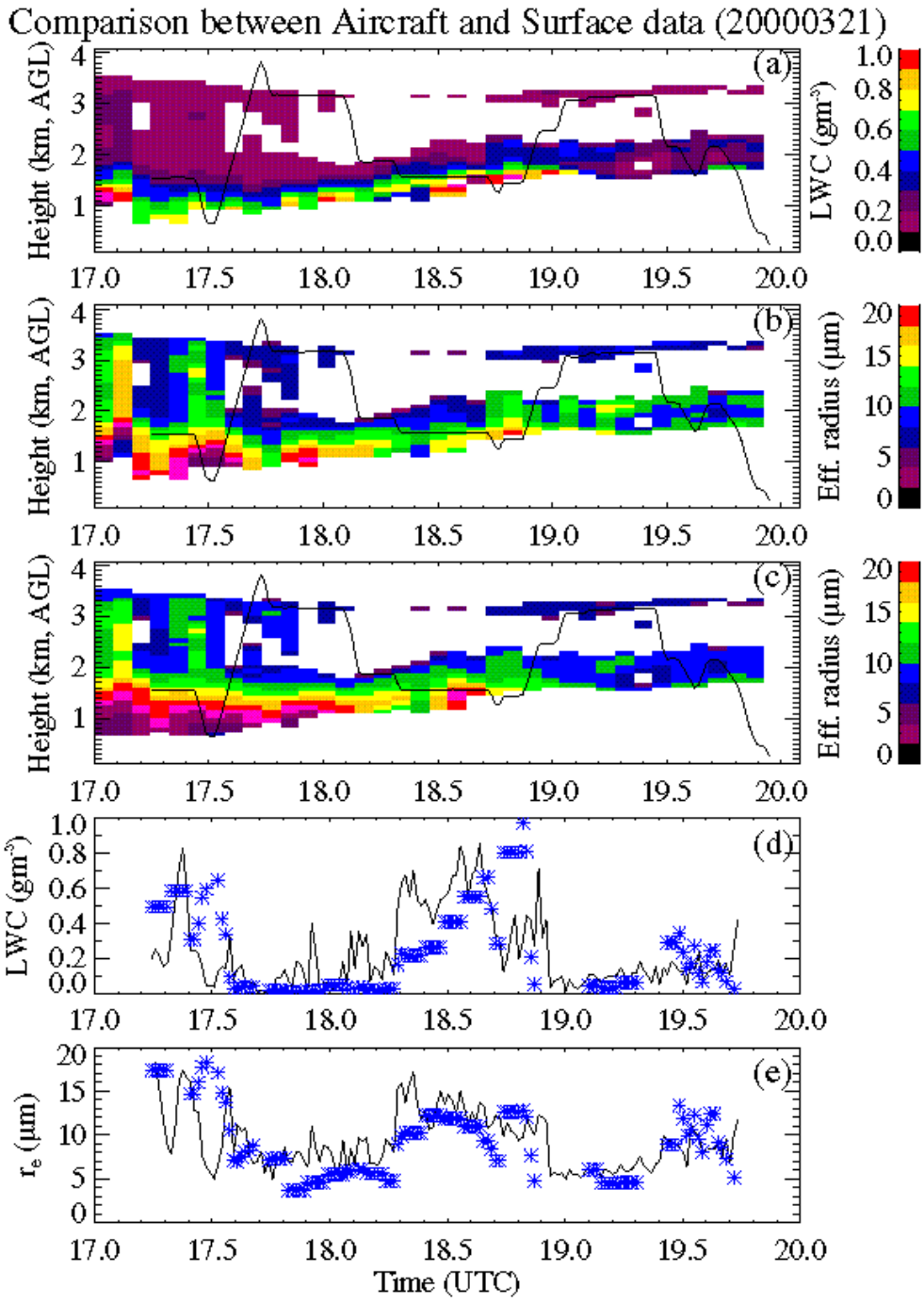
Comparison between Aircraft and Surface data (20000321)
(a)
(b)
(c)
(d)
(e)
Height (km, AGL)
LWC (gm^{-3})
Eff. radius (μm)
r_e (μm)
Time (UTC)
17.0
17.5
18.0
18.5
19.0
19.5
20.0

Figure 9

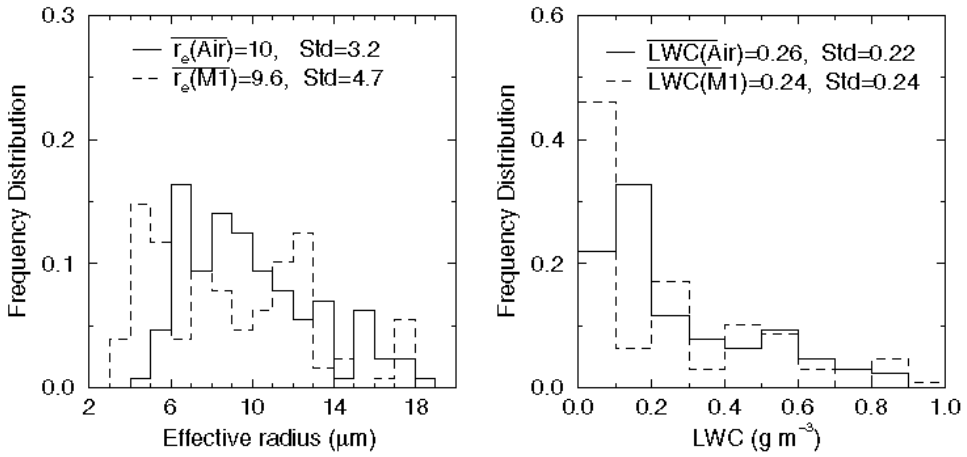
0.3
0.2
0.1
0.0
Frequency Distribution
$\overline{r_e}$(Air)=10, Std=3.2
$\overline{r_e}$(M1)=9.6, Std=4.7
2
6
10
14
18
Effective radius (μm)
0.6
0.4
0.2
0.0
Frequency Distribution
$\overline{LWC}$(Air)=0.26, Std=0.22
$\overline{LWC}$(M1)=0.24, Std=0.24
0.0
0.2
0.4
0.6
0.8
1.0
LWC (g m^{-3})

Figure 10

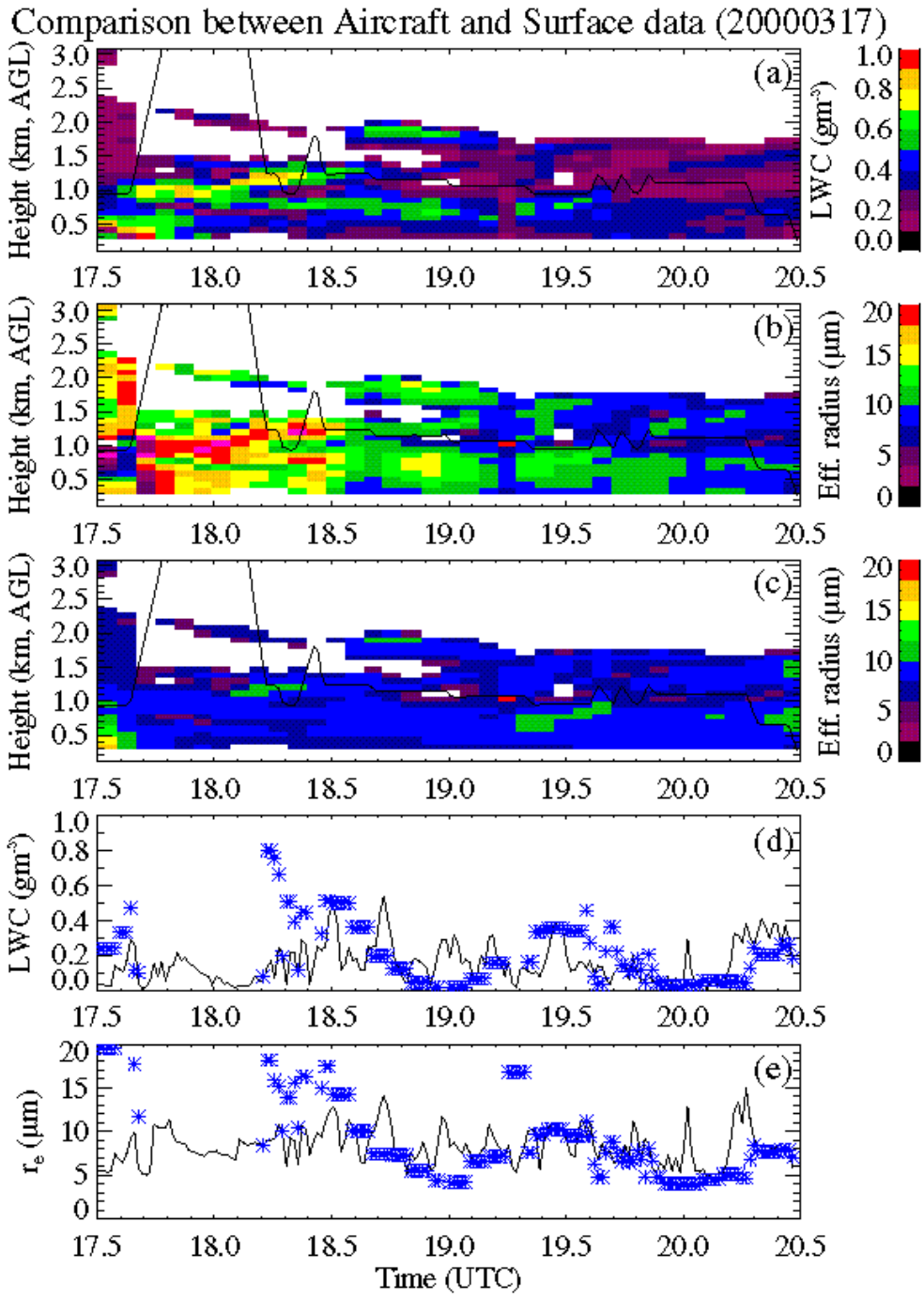
Comparison between Aircraft and Surface data (20000317)
Height (km, AGL)
LWC (gm-3)
Eff. radius (μm)
re (μm)
Time (UTC)
(a)
(b)
(c)
(d)
(e)

Figure 11

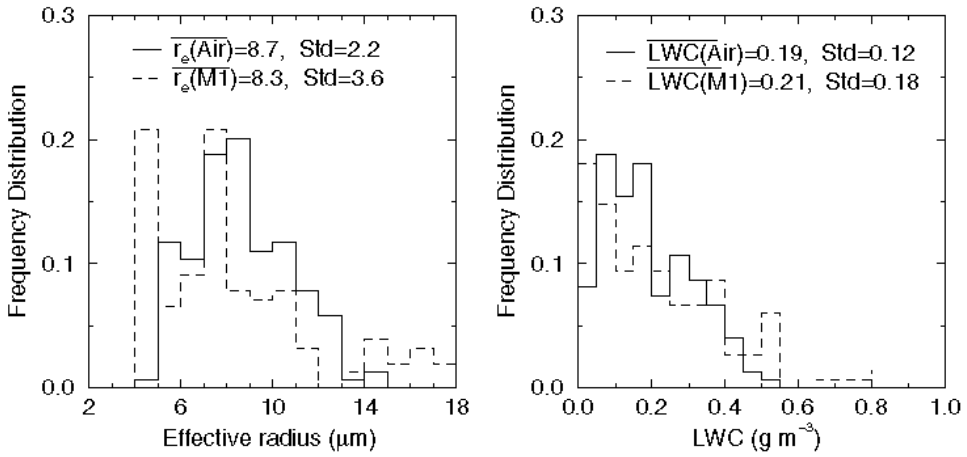
0.3
0.2
0.1
0.0
Frequency Distribution
$\overline{r_e}$(Air)=8.7, Std=2.2
$\overline{r_e}$(M1)=8.3, Std=3.6
2
6
10
14
18
Effective radius (μm)
$\overline{LWC}$(Air)=0.19, Std=0.12
$\overline{LWC}$(M1)=0.21, Std=0.18
0.0
0.2
0.4
0.6
0.8
1.0
LWC (g m^{-3})

Figure 12

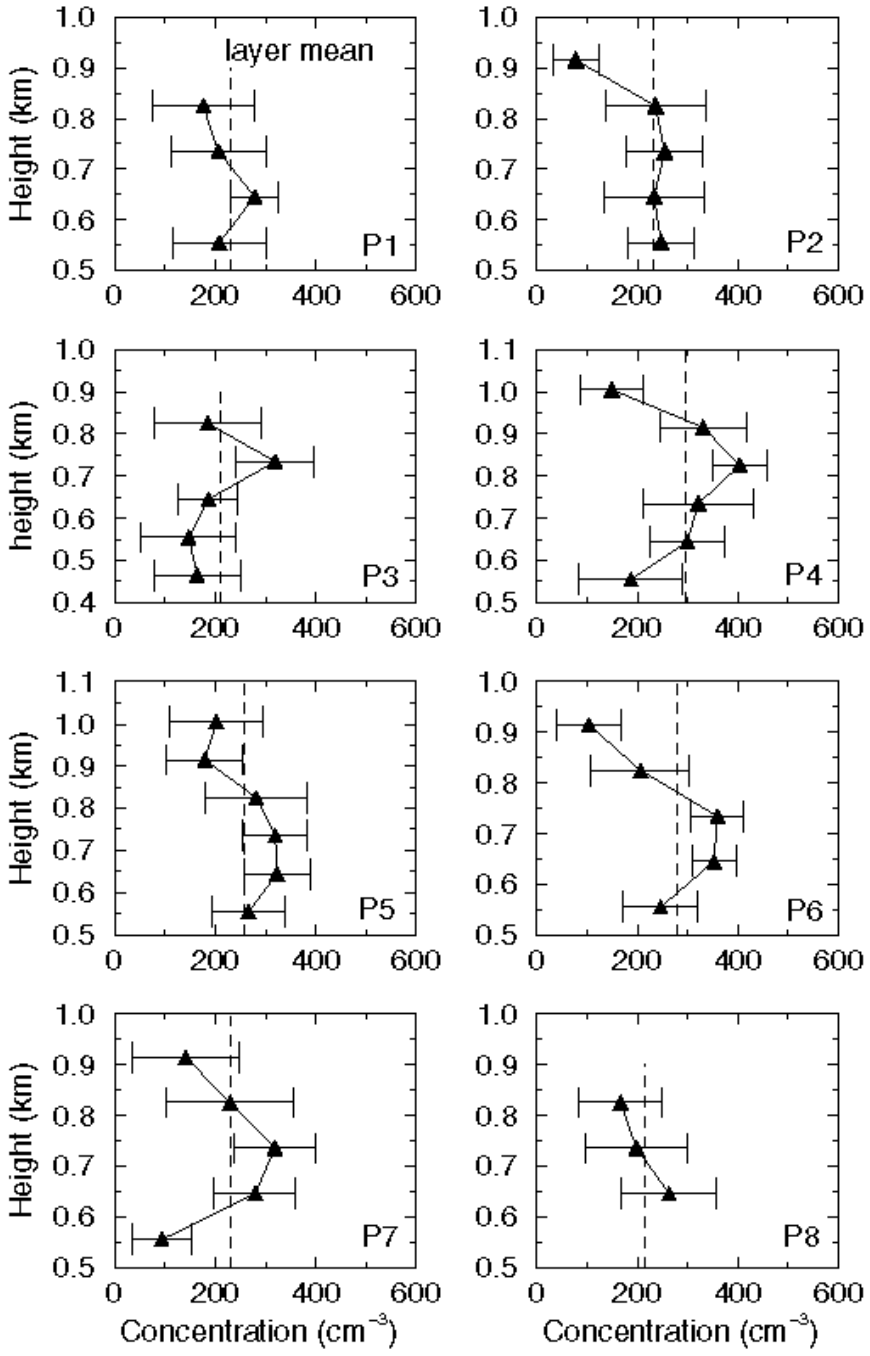
layer mean
P1
P2
P3
P4
P5
P6
P7
P8
Height (km)
height (km)
Concentration (cm^{-3})

Figure A1

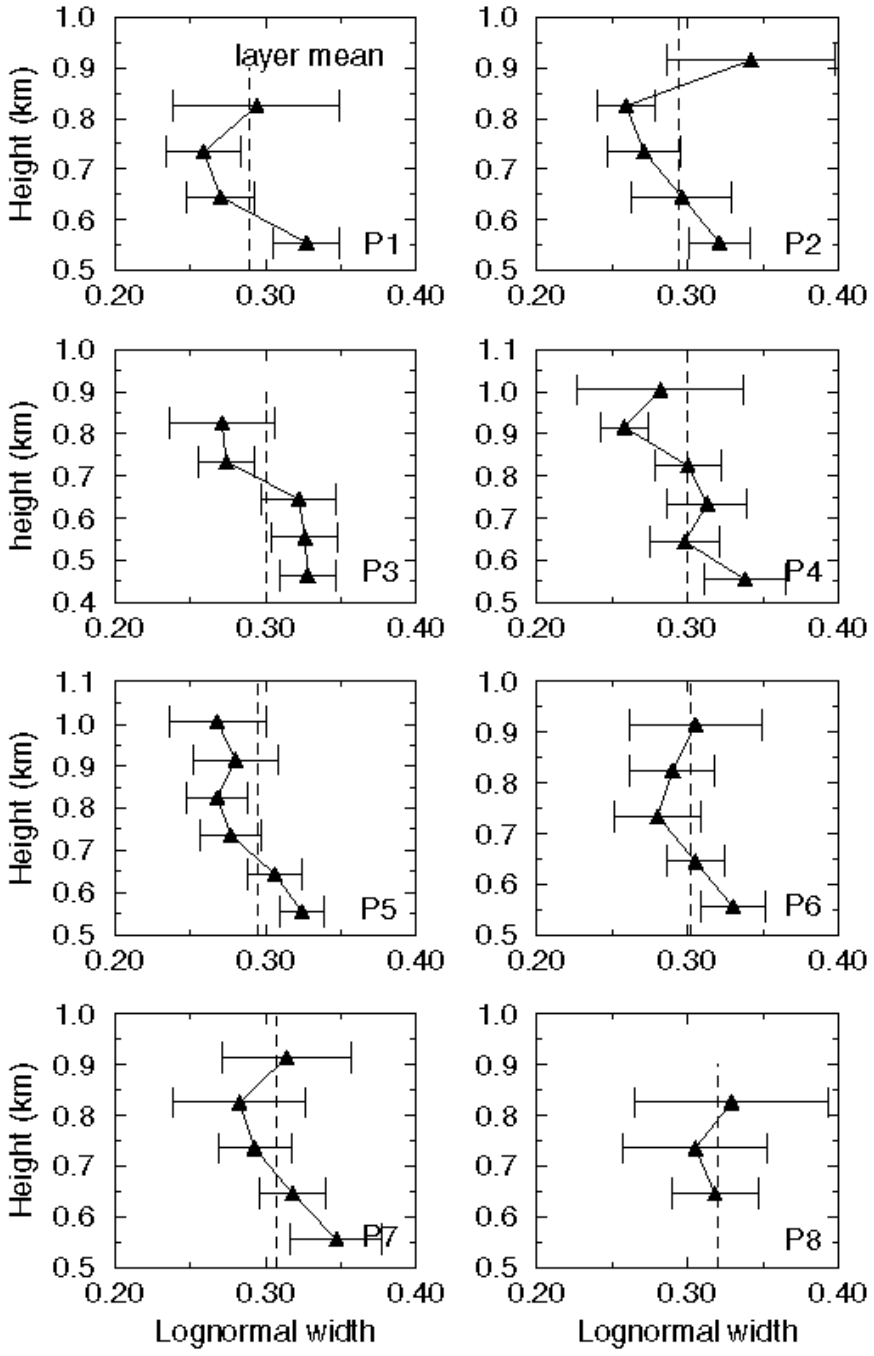
layer mean
P1
P2
P3
P4
P5
P6
P7
P8
Height (km)
height (km)
Lognormal width
Lognormal width

Figure A2